Smart Structures and Systems, *Vol. 26, No. 2 (2020) 157-174*
DOI: https://doi.org/10.12989/sss.2020.26.2.157

Guided wave field calculation in anisotropic layered structures using normal mode expansion method

Lingfang Li [1a], Hanfei Mei [2b], Mohammad Faisal Haider [3c], Dimitris Rizos [4d], Yong Xia*[1] and Victor Giurgiutiu [2e]

[1] *Department of Civil and Environmental Engineering, The Hong Kong Polytechnic University, Hung Hom, Kowloon, Hong Kong*
[2] *Department of Mechanical Engineering, University of South Carolina, Columbia, SC 29208, USA*
[3] *Department of Aeronautics and Astronautics, Stanford University, Stanford, CA 94305, USA*
[4] *Department of Civil Engineering, University of South Carolina, Columbia, SC 29208, USA*

(*Received September 10, 2019, Revised May 31, 2020, Accepted June 2, 2020*)

Abstract. The guided wave technique is commonly used in structural health monitoring as the guided waves can propagate far in the structures without much energy loss. The guided waves are conventionally generated by the surface-mounted piezoelectric wafer active sensor (PWAS). However, there is still lack of understanding of the wave propagation in layered structures, especially in structures made of anisotropic materials such as carbon fiber reinforced polymer (CFRP) composites. In this paper, the Rayleigh-Lamb wave strain tuning curves in a PWAS-mounted unidirectional CFRP plate are analytically derived using the normal mode expansion (NME) method. The excitation frequency spectrum is then multiplied by the tuning curves to calculate the frequency response spectrum. The corresponding time domain responses are obtained through the inverse Fourier transform. The theoretical calculations are validated through finite element analysis and an experimental study. The PWAS responses under the free, debonded and bonded CFRP conditions are investigated and compared. The results demonstrate that the amplitude and travelling time of wave packet can be used to evaluate the CFRP bonding conditions. The method can work on a baseline-free manner.

Keywords: guided waves; anisotropic; layered plate; piezoelectric wafer active sensor; normal mode expansion; debonding

1. Introduction

The guided wave technology (Su *et al*. 2006), which uses ultrasonic waves that can propagate far in the waveguide without much energy loss, is suitable for inspecting large areas of complicated structures and has gained wide attention from structural health monitoring (SHM) communities in recent decades. Guided waves are commonly excited by directly attached electromagnetic-acoustic transducers (Hirao 2017, Wilcox 2003) and piezoelectric transducers (Yu and Giurgiutiu 2008) or other non-contacting air-coupled transducers (Chimenti 2014). Among them, the piezoelectric wafer active sensor (PWAS) are commonly used to generate and receive guided waves in SHM applications due to the direct and converse piezoelectric effects (Meitzler *et al*. 1988). Contrary to the conventional transducers, PWASs are low cost, lightweight, and unobtrusive to the monitored structures. They can be permanently bonded to the host structures in large quantities and achieve real-time SHM. PWASs can be used in various modes, including pitch-catch, pulse-echo, phased array, and electromechanical impedance modes (Giurgiutiu 2007). Possible structural damage such as delamination, debonding, dents, and cracks, which change the waveguide properties and introduce wave scatters, can be detected by examining the changes in the wave amplitudes, packet shapes and the newly emerged wave packets (Lee *et al*. 2013, Shen and Giurgiutiu 2013, 2016, Wang *et al*. 2017).

In plate-like structures, the commonly used guided wave types include the Lamb and shear horizontal (SH) waves. Such waves are dispersive and contain multiple modes. The modes converge to Rayleigh/Love surface waves when the structure thickness or the frequency increases. Several efficient techniques have been developed to study the wave properties in structures. Explicit closed-form solutions for these steady state problems exist for structures made of isotropic materials. However, in structures made of anisotropic materials, the waves polarize in different directions, and are generally coupled except for in particular directions (Li and Thompson 1990). Mathematical tools become necessary in such cases. The generally available methods include the global matrix method (GMM) (Knopoff 1964, Lowe 1995), transfer matrix method (TMM) (Rose, 2014), stiffness matrix method (SMM) (Wang and Rokhlin 2001), elastodynamic finite integration technique (Leckey *et al*. 2014), spectral finite element method (Gopalakrishnan *et al*. 2011), 3-D elasticity theory method (Wang and Yuan 2007) and semi-analytical finite element (SAFE) (Loveday 2009, Velichko and Wilcox

*Corresponding author, Ph.D., Professor,
E-mail: y.xia@polyu.edu.hk
[a] Ph.D., E-mail: lingfang.li@connect.polyu.hk
[b] Ph.D. Candidate, E-mail: hmei@email.sc.edu
[c] Ph.D., E-mail: fhaider@stanford.edu
[d] Professor, E-mail: rizos@cec.sc.edu
[e] Professor, E-mail: victorg@sc.edu

http://www.techno-press.org/?journal=sss&subpage=7
ISSN: 1738-1584 (Print), 1738-1991 (Online)

2007, Zhang *et al*. 2018) method. These methods provide the stationary guided wave dispersion, phase velocity, group velocity and mode shape information in the frequency domain. The GMM, which is used in this paper, will be reminded again in Section 3.

The guided wave responses induced by transient excitations contain a broad frequency range due to the dispersive nature of the waves. They are typically analyzed in the frequency domain first and then transferred back into the time domain.

Several methods have been developed in the frequency domain to calculate the response of plates subjected to various types of external excitations. Green's function is suitable for calculating the wave field generated by point loads. For example, Bai *et al*. (2004) adopted it for obtaining the wave field in single- and multi-layer isotropic plates excited by point loads. Velichko and Wilcox (2007) studied the guided waves in generally anisotropic multi-layer plates. Glushkov *et al*. (2011) obtained the wave field and energy distribution due to point loads and ring delta-like surface tension in anisotropic laminate composites. Vrettos (2008) studied the wave field in an elastic half-space with depth-degrading stiffness excited by vertical point loads. When the excitation is applied on a finite zone, this method can also reach reasonable accuracy at relatively far field.

Several researchers (Giurgiutiu 2005, 2014, Kamal *et al*. 2014, Santoni and Giurgiutiu 2012, Shen and Giurgiutiu 2014) used the integral transform method (ITM) to obtain the tuning curves of the straight and circular crested waves subjected to surface mounted PWAS excitations in single-layer isotropic plates. The ITM first transforms the wave governing equations for the straight-crested (or circular-crested) wave equations into the wavenumber domain through Fourier transform (or Hankel transform). The wavenumber domain solutions are then transferred back to the physical domain through the corresponding inverse transforms. Complicated transform calculations are required among different domains in this method. Liu and Xi (2001) incorporated ITM with numerical approximation in the plate thickness direction and proposed a hybrid numerical method to apply the ITM to the composite plates. Barouni and Saravanos (2016) studied the surface-excited straight-crested waves in lamina and sandwiched plates with the ITM.

The normal mode expansion (NME) method is an analytical method that utilizes the orthogonality relations of Lamb wave modes avoiding, thus, the complicated transform calculations among domains. Using this method, Achenbach and Xu (1999) and Weaver and Pao (1982) predicted the wave field excited by a point source. Santoni (2010) approximated the tuning curve for circular-crested waves in isotropic plates (excited by the circular PWAS) without considering the decrease in wave amplitude. Li *et al*. (2019) extended this study to multi-layer isotropic plates by considering the decrease of amplitude. Moulin *et al*. (2000) calculated the straight-crested Lamb waves in single layer composite plates. Mei and Giurgiutiu (2018) also predicted the wave field in an anisotropic single-layer plate using the NME method in a semi-analytical manner.

Carbon fiber reinforced polymer (CFRP) composite plates are commonly used in civil engineering field to strengthen or retrofit concrete and steel structures (Petrou *et al*. 2008). Strengthening is effective only when the CFRP-structure bonding condition is secured. However, debonding can initiate at small cracks and bonding imperfections, and gradually propagate to other parts of the structure. Therefore, it is of vital importance to monitor the bonding condition. Guided wave technology could be utilized in this field since the bonding condition will alter the wave guide properties and thus the wave field (Mohseni and Ng 2013, 2019). Therefore, by examining wave field changes, the CFRP bonding conditions can be evaluated. For example, Ng and Veidt (2012) investigated the scattering characteristics of Lamb waves from a debonding at a structural feature in a composite laminate from the numerical and experimental aspects. Sherafat *et al*. (2016) evaluated the integrity of a composite skin-stringer joint using the scattering behavior of the Lamb waves experimentally. Leckey *et al*. (2018) compared the guided wave simulations for CFRP composites using four different simulation codes. These studies, despite considered the interaction between the wave fields and the debonding damage in the thin wall structures, were generally from the numerical and experimental aspects. The application of guided wave technique in the evaluation of the CFRP bonding condition in civil structures, which usually have large thickness, is still quite limited. There is a need to establish the theoretical basis of the wave field in the CFRP strengthened reinforced concrete (RC) structures under different bonding conditions before the technique can be widely used.

In this study, the NME method is developed to calculate the wave fields in CFRP plates generated by the surface mounted PWAS. The analytical results are validated by finite element analysis (FEA) and an experimental study. The PWAS responses in both bonded and debonded CFRP plates are also compared. The effectiveness of the guided waves for evaluating the CFRP bonding condition is thus demonstrated.

2. PWAS basis

Piezoelectric materials couple the mechanical and electrical fields through the direct and converse piezoelectric effects expressed in indicial notation as (Meitzler *et al*. 1988)

$$S_{ij} = s^E_{ijkl} T_{kl} + d_{kij} E_k \tag{1}$$

$$D_j = d_{jkl} T_{kl} + \varepsilon^T_{kl} E_k \tag{2}$$

where S_{ij} is the mechanical strain, T_{kl} the mechanical stress, E_k the electrical field, D_j the electrical displacement, s^E_{ijkl} the mechanical compliance of the material at zero electrical field (E = 0), d_{jkl} the piezoelectric coupling factor, and ε^E_{kl} the dielectric permittivity at zero mechanical stress field (T = 0). In a surface mounted PWAS configuration, the d_{31} piezoelectric coupling effect is utilized, i.e., the out-of-

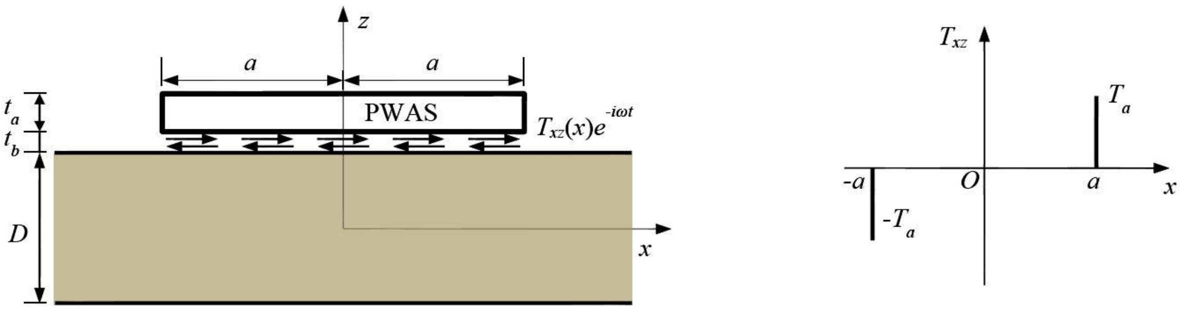

(a) Physical model (cross-section view) (b) Pin-force model

Fig. 1 Interaction between the PWAS and host structure (t_a: PWAS thickness, a: radius of circular PWAS, t_b: bond layer thickness, D: thickness of plate)

plane electrical field E_3 in the PWAS induces the in-plane strain, which will be transferred to the host structure through the adhesive layer (Giurgiutiu 2014, Santoni 2010) as shown in Fig. 1. It concentrates more near the PWAS border when the bonding layer is thinner. In the ideal case, the thickness of the bonding layer is neglected, which is referred to as the pin-force model as shown in Fig. 1(b). The equivalent effective stress of the pin-force model is given by Giurgiutiu (2014)

$$T_{xz}(x) = T_a[\delta(x-a) - \delta(x+a)] \tag{3}$$

$$T_a = \frac{\psi}{\psi+\alpha} t_a E_a \varepsilon_{ISA} \tag{4}$$

$$\psi = \frac{Eh}{E_a t_a} \tag{5}$$

$$\varepsilon_{ISA} = -\frac{d_{31}V}{t_a} \tag{6}$$

3. Guided wave basis in anisotropic materials

3.1 Stiffness matrix of generally anisotropic material

The stiffness matrix of the generally monoclinic materials, such as the commonly used composite materials, is given by

$$C = \begin{bmatrix} c_{11} & c_{12} & c_{13} & 0 & 0 & c_{16} \\ & c_{22} & c_{23} & 0 & 0 & c_{26} \\ & & c_{33} & 0 & 0 & c_{36} \\ & & & c_{44} & c_{45} & 0 \\ & symm. & & & c_{55} & 0 \\ & & & & & c_{66} \end{bmatrix} \tag{7}$$

The material stiffness can also be expressed by a fourth order stiffness tensor as c_{ijkl}, where $i, j, k, l = 1, 2, 3$. The tensors compare to the stiffness matrix components as

$$C = \begin{bmatrix} c_{1111} \to c_{11} & c_{1122} \to c_{12} & c_{1133} \to c_{13} & 0 & 0 & c_{1112} \to c_{16} \\ & c_{2222} \to c_{22} & c_{2233} \to c_{23} & 0 & 0 & c_{2212} \to c_{26} \\ & & c_{3333} \to c_{33} & 0 & 0 & c_{3312} \to c_{36} \\ & symm. & & c_{2323} \to c_{44} & c_{2313} \to c_{45} & 0 \\ & & & & c_{1313} \to c_{55} & 0 \\ & & & & & c_{1212} \to c_{66} \end{bmatrix} \tag{8}$$

where δ is the Dirac delta function, ψ is the stiffness factor with E and E_a being the Young's modulus of the plate and PWAS, respectively, and t and t_a being their thicknesses, ε_{ISA} is the induced strain with d_{31} being the piezoelectric factor and V the applied voltage, and factor α depends on the stress, strain and displacement distribution across the thickness. Under low frequency dynamic conditions, α takes the value of 4.

If the coordinate system rotates along the z-axis by an angle of θ, the new material stiffness matrix C' can be obtained as

$$C' = R^{-1} C R^{-T}, \tag{9}$$

$$R = \begin{bmatrix} \cos^2\theta & \sin^2\theta & 0 & 0 & 0 & 2\sin\theta\cos\theta \\ \sin^2\theta & \cos^2\theta & 0 & 0 & 0 & -2\sin\theta\cos\theta \\ 0 & 0 & 1 & 0 & 0 & 0 \\ 0 & 0 & 0 & \cos\theta & -\sin\theta & 0 \\ 0 & 0 & 0 & -\sin\theta & \cos\theta & 0 \\ -\sin\theta\cos\theta & \sin\theta\cos\theta & 0 & 0 & 0 & \cos^2\theta - \sin^2\theta \end{bmatrix} \tag{10}$$

where R is the θ-dependent 3 dimensional transformation matrix and the superscript T is the transpose of a matrix.

3.2 Wave propagation in bulk anisotropic material

Assume a plane harmonic wave of frequency ω propagates in a general anisotropic material in the direction $\vec{n} = n_x\overrightarrow{e_x} + n_y\overrightarrow{e_y} + n_z\overrightarrow{e_z}$ with speed c and corresponding wavenumber $\xi = \omega/c$. Then the wavenumber vector is $\vec{k} = k_x\overrightarrow{e_x} + k_y\overrightarrow{e_y} + k_z\overrightarrow{e_z}$, where k_x, k_y, and k_z are the directional wavenumbers and represent the projections of the wavenumber vector $\vec{k}$ in the x, y, and z directions. Therefore, the particle displacement can be written as

$$\vec{u}(\vec{r},t) = \hat{u}e^{i(\vec{k}\cdot\vec{r}-\omega t)} = \hat{u}e^{i(k_x\overrightarrow{e_x}+k_y\overrightarrow{e_y}+k_z\overrightarrow{e_z}-\omega t)} \quad (11)$$

where $\vec{r}$ is the location vector and t is time. Eq. (11) can be rewritten as

$$\begin{Bmatrix} u_x \\ u_y \\ u_z \end{Bmatrix} = \begin{Bmatrix} \hat{u}_x \\ \hat{u}_y \\ \hat{u}_z \end{Bmatrix} e^{i(k_x\overrightarrow{e_x}+k_y\overrightarrow{e_y}+k_z\overrightarrow{e_z}-\omega t)} \quad (12)$$

where $\widehat{u_x}$, $\widehat{u_y}$ and $\widehat{u_z}$ are the complex displacement magnitudes in the x, y and z directions.

3.3 Wave field in a lamina of finite thickness

3.3.1 Displacement field

Consider the N-layer laminated structure of thickness D shown in Fig. 2. The coordinate system is such chosen that the x-axis is the direction of propagation of the wave of angular frequency ω, wavenumber ξ and phase velocity $c = \omega/\xi$. The z-axis is along the thickness of the laminated structure and the bottom surface is at $z = 0$. The guided wave propagation is contained in the vertical plane xOz and the problem is y-invariant. The wavenumber in the z-direction is $k_z = \alpha\xi$ where $\alpha = k_z/k_x$. Under these assumptions the displacement field in Eq. (12) is simplified into

$$\begin{Bmatrix} u_x \\ u_y \\ u_z \end{Bmatrix} = \begin{Bmatrix} \hat{u}_x \\ \hat{u}_y \\ \hat{u}_z \end{Bmatrix} e^{i\xi(x+\alpha z-ct)} \quad (13)$$

The equation of motion in terms of displacements is expressed as

$$c_{ijlm}u_{m,lj} = \rho\ddot{u}_i, \qquad i = 1,2,3\ (x,y,z) \quad (14)$$

where ρ is the material density and double dots indicate derivatives with respect to time. By substituting the material stiffness matrix, Eq. (7), into Eq. (14) becomes

$$\begin{aligned} \rho\ddot{u}_x &= c_{11}u_{x,xx} + c_{55}u_{x,zz} + c_{16}u_{y,xx} \\ &\quad + c_{45}u_{y,xx} + c_{13}u_{z,zx} + c_{55}u_{z,zx} \\ \rho\ddot{u}_y &= c_{16}u_{x,xx} + c_{45}u_{x,zz} + c_{66}u_{y,xx} \\ &\quad + c_{44}u_{y,xx} + c_{36}u_{z,zx} + c_{45}u_{z,zx} \\ \rho\ddot{u}_z &= c_{55}u_{x,xz} + c_{31}u_{x,xz} + c_{45}u_{y,xz} \\ &\quad + c_{36}u_{y,zx} + c_{55}u_{z,xx} + c_{33}u_{z,zz} \end{aligned} \quad (15)$$

Substituting Eq. (13) in Eq. (15) and taking derivatives with respect to x yields

$$\begin{bmatrix} c_{11}+c_{55}\alpha^2-\rho c^2 & c_{16}+c_{45}\alpha^2 & (c_{13}+c_{55})\alpha \\ c_{16}+c_{45}\alpha^2 & c_{66}+c_{44}\alpha^2-\rho c^2 & (c_{16}+c_{45})\alpha \\ (c_{13}+c_{55})\alpha & (c_{16}+c_{45})\alpha & c_{55}+c_{33}\alpha^2-\rho c^2 \end{bmatrix} \cdot \begin{Bmatrix} \hat{u}_x \\ \hat{u}_y \\ \hat{u}_z \end{Bmatrix} = \begin{Bmatrix} 0 \\ 0 \\ 0 \end{Bmatrix} \quad (16)$$

Non-trivial solutions exist only when the determinant of the matrix is zero, i.e.

$$\begin{vmatrix} c_{11}+c_{55}\alpha^2-\rho c^2 & c_{16}+c_{45}\alpha^2 & (c_{13}+c_{55})\alpha \\ c_{16}+c_{45}\alpha^2 & c_{66}+c_{44}\alpha^2-\rho c^2 & (c_{16}+c_{45})\alpha \\ (c_{13}+c_{55})\alpha & (c_{16}+c_{45})\alpha & c_{55}+c_{33}\alpha^2-\rho c^2 \end{vmatrix} = 0 \quad (17)$$

Eq. (17) is a six-order polynomial equation of α, or a bicubic equation of α^2. It has three pairs of solutions, i.e., $\pm\alpha_I$, $\pm\alpha_{II}$ and $\pm\alpha_{III}$. The positive roots corresponds to waves with increasing amplitude as z increases while the negative to wave with decreasing amplitudes. Each α, corresponds to a singular displacement eigenvector in the form of $U_{3\times 1}^{(i)}$ (i = 1, 2 , 3, …, 6). The total possible partial wave solutions are

$$\begin{aligned} \alpha &= \{\alpha_1 \quad \alpha_2 \quad \alpha_3 \quad \alpha_4 \quad \alpha_5 \quad \alpha_6\}^T \\ &= \{\alpha_I \quad -\alpha_I \quad \alpha_{II} \quad -\alpha_{II} \quad \alpha_{III} \quad -\alpha_{III}\}^T \end{aligned} \quad (18)$$

and

$$U = [U^{(1)} \quad U^{(2)} \quad U^{(3)} \quad U^{(4)} \quad U^{(5)} \quad U^{(6)}]_{3\times 6}^T \quad (19)$$

Substituting Eqs. (18) and (19) into Eq. (13), the wave field becomes

$$u = \hat{u}(z)e^{i\xi(x-ct)} = \left(\sum_{j=1}^{6} \eta_j U^{(j)} e^{i\xi\alpha_j z}\right) e^{i\xi(x-ct)} \quad (20)$$

where η_j (j = 1, 2, …, 6) are the partial wave participation factors. The z-dependent part of Eq. (20) can be rearranged as

$$\hat{\boldsymbol{u}}(\boldsymbol{z}) = \boldsymbol{B_u}(\boldsymbol{z})\boldsymbol{\eta} \quad (21)$$

where $B_u(z) = \left[b_u^{(1)} \quad b_u^{(2)} \quad b_u^{(3)} \quad b_u^{(4)} \quad b_u^{(5)} \quad b_u^{(6)}\right]$ is the z-dependent displacement matrix with $\eta = \{\eta_1 \quad \eta_2 \quad \eta_3 \quad \eta_4 \quad \eta_5 \quad \eta_6\}^T$ being the partial wave participation factor vector and $b_u^{(j)}(z) = U^{(j)}e^{i\xi\alpha_j z}$.

3.3.2 Stress field

The stress-displacement relations under the y-invariant condition is expressed as

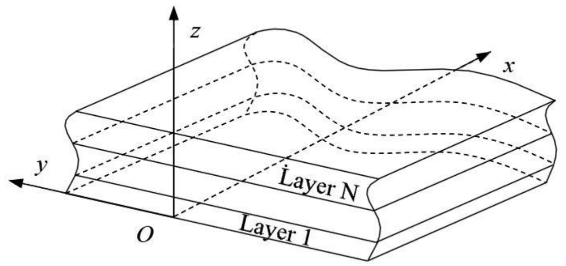

Fig. 2 N-layer laminated structure

3.4 Wave field in a lamina of infinite thickness

3.4.1 Displacement field

When the thickness of the lamina increases, the Lamb waves converge to the Rayleigh waves, which appear mainly on the surface of the half-space and decay in the depth direction. The Rayleigh wave fields can be obtained through the same procedures as the Lamb wave fields in structures of finite thickness. In view of the structure and coordinate system shown in Fig. 2, the case for which $D = \infty$ represents the layered half space. In this case the waves attenuate as $z \to \infty$. Similar with the Lamb wave field analysis in Eq. (17), only its negative roots of α satisfy the condition and the positive roots of α do not contribute to the attenuation in the z-direction (depth). The negative roots are

$$\begin{Bmatrix}\sigma_{xx}\\ \sigma_{yy}\\ \sigma_{zz}\\ \sigma_{yz}\\ \sigma_{xz}\\ \sigma_{xy}\end{Bmatrix} = \begin{bmatrix} c_{11} & c_{12} & c_{13} & 0 & 0 & c_{16}\\ & c_{22} & c_{23} & 0 & 0 & c_{26}\\ & & c_{33} & 0 & 0 & c_{36}\\ & & & c_{44} & c_{45} & 0\\ & \text{symm.} & & & c_{55} & 0\\ & & & & & c_{66}\end{bmatrix} \begin{Bmatrix} u_{x,x}\\ 0\\ u_{z,z}\\ u_{y,z}\\ u_{x,z}+u_{z,x}\\ u_{y,z}\end{Bmatrix} \tag{22}$$

Substituting Eq. (20) into Eq. (22), the interface traction components become

$$\begin{aligned}
\hat{\sigma}_{xz} &= c_{55} i\xi \sum_{j=1}^{6} \alpha_j \eta_j U_x^{(j)} e^{i\xi\alpha_j z} \\
&+ c_{55} i\xi \sum_{j=1}^{6} \eta_j U_z^{(j)} e^{i\xi\alpha_j z} + c_{45} i\xi \sum_{j=1}^{6} \alpha_j \eta_j U_y^{(j)} e^{i\xi\alpha_j z} \\
&= i\xi \sum_{j=1}^{6} \left(c_{55}\alpha_j U_x^{(j)} + c_{55} U_z^{(j)} + c_{45}\alpha_j U_y^{(j)} \right) \eta_j e^{i\xi\alpha_j z} \\
\hat{\sigma}_{yz} &= c_{45} i\xi \sum_{j=1}^{6} \alpha_j \eta_j U_x^{(j)} e^{i\xi\alpha_j z} \\
&+ c_{45} i\xi \sum_{j=1}^{6} \eta_j U_z^{(j)} e^{i\xi\alpha_j z} + c_{44} i\xi \sum_{j=1}^{6} \alpha_j \eta_j U_y^{(j)} e^{i\xi\alpha_j z} \\
&= i\xi \sum_{j=1}^{6} \left(c_{45}\alpha_j U_x^{(j)} + c_{45} U_z^{(j)} + c_{44}\alpha_j U_y^{(j)} \right) \eta_j e^{i\xi\alpha_j z} \\
\hat{\sigma}_{zz} &= c_{13} i\xi \sum_{j=1}^{6} \eta_j U_x^{(j)} e^{i\xi\alpha_j z} \\
&+ c_{33} i\xi \sum_{j=1}^{6} \eta_j \alpha_j U_z^{(j)} e^{i\xi\alpha_j z} + c_{36} i\xi \sum_{j=1}^{6} \eta_j U_y^{(j)} e^{i\xi\alpha_j z} \\
&= i\xi \textstyle\sum_{j=1}^{6} \left(c_{13} U_x^{(j)} + c_{33}\alpha_j U_z^{(j)} + c_{36} U_y^{(j)} \right) \eta_j e^{i\xi\alpha_j z}
\end{aligned} \tag{23}$$

Eq. (23) can be written in a matrix form as

$$\hat{\sigma}(z) = \begin{Bmatrix} \hat{\sigma}_{xz}(z) \\ \hat{\sigma}_{yz}(z) \\ \hat{\sigma}_{zz}(z) \end{Bmatrix} = B_\sigma(z) \tag{24}$$

with $B_\sigma(z) = \left[b_\sigma^{(1)} \quad b_\sigma^{(2)} \quad b_\sigma^{(3)} \quad b_\sigma^{(4)} \quad b_\sigma^{(5)} \quad b_\sigma^{(6)} \right]$ and

$$\boldsymbol{b}_{\sigma}^{(j)}(\boldsymbol{z}) = \boldsymbol{i\xi} \begin{Bmatrix} \boldsymbol{c_{55}\alpha_j U_x^{(j)} + c_{55} U_z^{(j)} + c_{45}\alpha_j U_y^{(j)}} \\ \boldsymbol{c_{45}\alpha_j U_x^{(j)} + c_{45} U_z^{(j)} + c_{44}\alpha_j U_y^{(j)}} \\ \boldsymbol{c_{13} U_x^{(j)} + c_{33}\alpha_j U_z^{(j)} + c_{36} U_y^{(j)}} \end{Bmatrix} \boldsymbol{e^{i\xi\alpha_j z}} \tag{25}$$

$j = 1, 2, \ldots, 6$

$$\alpha = \{-\alpha_I \quad -\alpha_{II} \quad -\alpha_{III}\}^T \tag{26}$$

and the corresponding eigenvectors become

$$U = [U^{(1)} \quad U^{(2)} \quad U^{(3)}]_{3\times3}^T. \tag{27}$$

The displacement field becomes

$$u = \hat{u}(z) e^{i\xi(x-ct)} = \left(\sum_{j=1}^{3} \eta_j U^{(j)} e^{i\xi\alpha_j z} \right) e^{i\xi(x-ct)} \tag{28}$$

$j = 1, 2, 3$

The z-dependent part of Eq. (28) can be rearranged as

$$u(z) = B_u(z)\eta \tag{29}$$

where $B_u(z) = \left[b_u^{(1)}(z) \quad b_u^{(2)}(z) \quad b_u^{(3)}(z) \right]$ is the new z-dependent displacement matrix with $b_u^{(j)}(z) = U^{(j)} e^{i\xi\alpha_j z}$ and $\eta = \{\eta_1 \quad \eta_2 \quad \eta_3\}^T$.

3.4.2 Stress field

According to the stress–displacement relation given in Eq. (22), the stresses are

$$\begin{aligned}
\hat{\sigma}_{xz} &= c_{55} i\xi \sum_{j=1}^{3} \alpha_j \eta_j U_x^{(j)} e^{i\xi\alpha_j z} \\
&+ c_{55} i\xi \sum_{j=1}^{3} \eta_j U_z^{(j)} e^{i\xi\alpha_j z} + c_{45} i\xi \sum_{j=1}^{3} \alpha_j \eta_j U_y^{(j)} e^{i\xi\alpha_j z} \\
&= i\xi \textstyle\sum_{j=1}^{3} \left(c_{55}\alpha_j U_x^{(j)} + c_{55} U_z^{(j)} + c_{45}\alpha_j U_y^{(j)} \right) \eta_j e^{i\xi\alpha_j z}
\end{aligned} \tag{30}$$

$$\hat{\sigma}_{yz} = c_{45} i\xi \sum_{j=1}^{3} \alpha_j \eta_j U_x^{(j)} e^{i\xi\alpha_j z} \tag{31}$$

$$+c_{45}i\xi\sum_{j=1}^{3}\eta_j U_z^{(j)}\,e^{i\xi\alpha_j z}+c_{44}i\xi\sum_{j=1}^{3}\alpha_j\eta_j U_y^{(j)}\,e^{i\xi\alpha_j z}$$
$$=i\xi\sum_{j=1}^{3}\left(c_{45}\alpha_j U_x^{(j)}+c_{45}U_z^{(j)}+c_{44}\alpha_j U_y^{(j)}\right)\eta_j e^{i\xi\alpha_j z} \tag{31}$$

$$\hat{\sigma}_{zz}=c_{13}i\xi\sum_{j=1}^{3}\eta_j U_x^{(j)}\,e^{i\xi\alpha_j z}$$
$$+c_{33}i\xi\sum_{j=1}^{3}\eta_j\alpha_j U_z^{(j)}\,e^{i\xi\alpha_j z}+c_{36}i\xi\sum_{j=1}^{3}\eta_j U_y^{(j)}\,e^{i\xi\alpha_j z}$$
$$=i\xi\sum_{j=1}^{3}\left(c_{13}U_x^{(j)}+c_{33}\alpha_j U_z^{(j)}+c_{36}U_y^{(j)}\right)\eta_j e^{i\xi\alpha_j z} \tag{32}$$

The above equations can be rewritten in the matrix form as

$$\hat{\sigma}(z)=\begin{Bmatrix}\hat{\sigma}_{xz}(z)\\ \hat{\sigma}_{yz}(z)\\ \hat{\sigma}_{zz}(z)\end{Bmatrix}=B_\sigma(z)\eta \tag{33}$$

with

$$B_\sigma=\left[b_\sigma^{(1)}(z)\quad b_\sigma^{(2)}(z)\quad b_\sigma^{(3)}(z)\right] \tag{34}$$

and

$$b_\sigma^{(j)}(z)=i\xi\begin{Bmatrix}c_{55}\alpha_j U_x^{(j)}+c_{55}U_z^{(j)}+c_{45}\alpha_j U_y^{(j)}\\ c_{45}\alpha_j U_x^{(j)}+c_{45}U_z^{(j)}+c_{44}\alpha_j U_y^{(j)}\\ c_{13}U_x^{(j)}+c_{33}\alpha_j U_z^{(j)}+c_{36}U_y^{(j)}\end{Bmatrix}e^{i\xi\alpha_j z} \tag{35}$$
$$j=1,2,3$$

3.5 Wave field in laminated structure

With the displacement and stress field equations given in the previous sections, the wave field equation of the laminated structure can be assembled by imposing the stress and displacement boundary conditions:

- Traction free conditions at the free surface(s) and
- Compatibility of displacements and stress equilibrium at the lamina interface.

If the N^{th} layer is of infinite thickness, the displacement and stress at infinity should vanish.

The wave field equation for the entire laminate structure can be established with the TMM, GMM or SMM in the general form of

$$\boldsymbol{B\Psi}=\{\mathbf{0}\} \tag{36}$$

in which $\boldsymbol{B}$ is the transfer, global, or stiffness matrix, depending on the method used, and $\boldsymbol{\Psi}$ is the global partial wave participation factor vector formed by the partial wave participation factor vectors $\boldsymbol{\eta}$ of all layers.

Non-trivial solutions exist only when the determinant of the matrix $\boldsymbol{B}$ is zero, i.e.

$$|B(\xi,\omega)|=0 \tag{37}$$

Eq. (37) is a homogenous equation that depends on two of three unknowns: the x-wave number ξ, the x-wave speed c, and the frequency ω. due to $c=\omega/\xi$. The equation also incorporates the partial-wave eigenvalues α_j and eigenvectors (or partial wave polarization vectors) $\boldsymbol{U}^{(j)}$ (j = 1, 2, …, 6), which can be obtained by solving Eq. (17) at different velocities. The (ξ, ω) or (ω, c) dispersion curves and the corresponding non-trivial solution of $\boldsymbol{\Psi}$ are then calculated with initial guesses and root-searching process. By substituting the element values of $\boldsymbol{\Psi}$ back to Eqs. (21) and (24), the corresponding displacement/stress mode shapes are obtained. According to the velocity-displacement relation, the velocity mode shapes are then obtained. Under the y-invariant assumption, the velocity and stress mode shapes are simplified as

$$\begin{aligned}v_x(x,z)&=v_x(z)e^{i\xi x}\\ v_z(x,z)&=v_z(z)e^{i\xi x}\\ \sigma_{xx}(x,z)&=\sigma_{xx}(z)e^{i\xi x}\\ \sigma_{xz}(x,z)&=\sigma_{xz}(z)e^{i\xi x}\\ \sigma_{zz}(x,z)&=\sigma_{zz}(z)e^{i\xi x}\end{aligned} \tag{38}$$

The dispersion curve and mode shapes of anisotropic materials are direction dependent. They can be calculated in the same way after rotating the coordinate system and updating the stiffness matrix. The wave field should be analyzed in each individual direction. More details are described in Section 5.

It is worth noting that there is no closed-form solution available in the calculation of the dispersion curves and mode shapes due to the anisotropic nature of the composites. Instead, the singular value decomposition is conducted to approximate the most accurate solution, in which errors may be introduced and accumulated.

4. Reciprocity relation and normal mode expansion

4.1 Elastodynamic reciprocity relation

Assume $\boldsymbol{U}_{12}$ is the displacement at point 1 due to force $\boldsymbol{F}_2$ at point 2 and $\boldsymbol{U}_{21}$ is the displacement at point 2 due to force $\boldsymbol{F}_1$ at point 1. The reciprocity relation states that the work done by $\boldsymbol{F}_1$ upon displacement $\boldsymbol{U}_{12}$ equals the work by $\boldsymbol{F}_2$ upon $\boldsymbol{U}_{21}$ (Santoni 2010), that is

$$\boldsymbol{F_1}\cdot\boldsymbol{U_{12}}=\boldsymbol{F_2}\cdot\boldsymbol{U_{21}} \tag{39}$$

The two forces generate velocity fields $\boldsymbol{V}_1$ and $\boldsymbol{V}_2$ and stress fields $\boldsymbol{T}_1$ and $\boldsymbol{T}_2$. Then, the complex reciprocity relation (Auld 1990) is

$$\nabla(\widetilde{V_2}\cdot T_1+V_1\cdot\widetilde{T_2})=-(\widetilde{V_2}\cdot F_1+V_1\cdot\widetilde{F_2}) \tag{40}$$

where the overhead tilde "~" stands for the complex conjugate of the corresponding term. For the straight-crested waves the complex reciprocity relation (Kamal *et al*. 2014) is

$$\frac{\partial}{\partial x}\left(\widetilde{V_x^2}T_{xx}^1+\widetilde{V_z^2}T_{xz}^1+V_x^1\widetilde{T_{xx}^2}+V_z^1\widetilde{T_{xz}^2}\right) \tag{41}$$

$$+\frac{\partial}{\partial z}\left(\widetilde{V_x^2}T_{xz}^1+\widetilde{V_z^2}T_{zz}^1+V_x^1\widetilde{T_{xz}^2}+V_z^1\widetilde{T_{zz}^2}\right)$$
$$=-\widetilde{V_x^2}F_x^1-V_x^1\widetilde{F_x^2}-\widetilde{V_z^2}F_z^1-V_z^1\widetilde{F_z^2} \tag{41}$$

where the superscripts "1" and "2" respectively indicate the wave fields generated by the external excitations $\boldsymbol{F}_1$ and $\boldsymbol{F}_2$.

4.2 Orthogonality relation

If the multi-layer structure is free from external excitations, i.e., $F_x^1=F_x^2=F_z^1=F_z^2=0$. The two wave fields can be considered two free wave modes. Without losing generality, the two harmonic wave fields are assumed as the m^{th} and n^{th} modes. Then the wave field in Eq. (41) becomes

$$\begin{aligned}&\frac{\partial}{\partial x}\left(\widetilde{v_x^n}\sigma_{xx}^m+\widetilde{v_z^n}\sigma_{xz}^m+v_x^m\widetilde{\sigma_{xx}^n}+v_z^m\widetilde{\sigma_{xz}^n}\right)\\&+\frac{\partial}{\partial z}\left(\widetilde{v_x^n}\sigma_{xz}^m+\widetilde{v_z^n}\sigma_{zz}^m+v_x^m\widetilde{\sigma_{xz}^n}+v_z^m\widetilde{\sigma_{zz}^n}\right)=0\end{aligned} \tag{42}$$

The above equation is integrated with respect to z along the entire thickness D, that is

$$\begin{aligned}&i\left(\xi_m-\widetilde{\xi_n}\right)e^{i(\xi_m-\widetilde{\xi_n})x}\\&\times\int_0^D\left(\widetilde{v_x^n}\sigma_{xx}^m+\widetilde{v_z^n}\sigma_{xz}^m+v_x^m\widetilde{\sigma_{xx}^n}+v_z^m\widetilde{\sigma_{xz}^n}\right)dz\\&+\left(\widetilde{v_x^n}\sigma_{xz}^m+\widetilde{v_z^n}\sigma_{zz}^m+v_x^m\widetilde{\sigma_{xz}^n}+v_z^m\widetilde{\sigma_{zz}^n}\right)e^{i(\xi_m-\widetilde{\xi_n})x}\Big|_0^D=0\end{aligned} \tag{43}$$

The common term $e^{i(\xi_m-\tilde{\xi}_n)x}$ can be cancelled out, which leads to

$$\begin{aligned}&i\left(\xi_m-\widetilde{\xi_n}\right)\\&\times\int_0^D\left(\widetilde{v_x^n}\sigma_{xx}^m+\widetilde{v_z^n}\sigma_{xz}^m+v_x^m\widetilde{\sigma_{xx}^n}+v_z^m\widetilde{\sigma_{xz}^n}\right)dz\\&+\left(\widetilde{v_x^n}\sigma_{xz}^m+\widetilde{v_z^n}\sigma_{zz}^m+v_x^m\widetilde{\sigma_{xz}^n}+v_z^m\widetilde{\sigma_{zz}^n}\right)\Big|_0^D=0\end{aligned} \tag{44}$$

For the traction-free surface conditions, i.e., $\sigma_{zz}=\sigma_{xz}=0$, Eq. (44) becomes

$$\begin{aligned}&i\left(\xi_m-\widetilde{\xi_n}\right)\\&\times\int_0^D\left(\widetilde{v_x^n}\sigma_{xx}^m+\widetilde{v_z^n}\sigma_{xz}^m+v_x^m\widetilde{\sigma_{xx}^n}+v_z^m\widetilde{\sigma_{xz}^n}\right)dz=0\end{aligned} \tag{45}$$

In this study, propagating modes with pure real wavenumbers are considered, i.e., evanescent waves are not considered as they will decay out with distance. In this case, when the wavenumber $\xi_m\neq\xi_n$, then

$$\int_0^D\left(\widetilde{v_x^n}\sigma_{xx}^m+\widetilde{v_z^n}\sigma_{xz}^m+v_x^m\widetilde{\sigma_{xx}^n}+v_z^m\widetilde{\sigma_{xz}^n}\right)dz=0 \tag{46}$$

Eq. (46) is the orthogonality relation of Lamb waves. Define $P_{mn}=\int_0^D\left(\widetilde{v_x^n}\sigma_{xx}^m+\widetilde{v_z^n}\sigma_{xz}^m+v_x^m\widetilde{\sigma_{xx}^n}+v_z^m\widetilde{\sigma_{xz}^n}\right)dz$, then $P_{mn}=0$ for $m\neq n$. Therefore the modes are referred to as "normal modes".

4.3 Normal mode expansion of Lamb waves

In the NME theory, the actual wave field generated by external excitations is a linear combination of the normal modes with their respective participation factors. With the mode shapes in the desired direction obtained from the matrix methods, the participation factors will be calculated in the following sections.

Assume the excitation $\boldsymbol{F}_2$ does not exist. Then the $\boldsymbol{F}_2$-induced wave field could be any free mode. Without losing generality, the wave field is assumed to be the n^{th} free mode, i.e.

$$\begin{aligned}V_x^2(x,z)&=v_x^n(z)e^{i\xi_nx}\\V_z^2(x,z)&=v_z^n(z)e^{i\xi_nx}\\T_{xx}^2(x,z)&=\sigma_{xx}^n(z)e^{i\xi_nx}\\T_{xz}^2(x,z)&=\sigma_{xz}^n(z)e^{i\xi_nx}\\T_{zz}^2(x,z)&=\sigma_{zz}^n(z)e^{i\xi_nx}\end{aligned} \tag{47}$$

Let the excitation $\boldsymbol{F}_1$ be the excitation of the surface mounted PWAS of infinite length, which means $F_x^1=F_z^1=0$ and the y-invariant condition is applicable. The wave fields are then assumed as

$$\begin{aligned}V_x^1(x,z)&=\sum a_m(x)\,v_x^m(z)e^{i\xi_mx}\\V_z^1(x,z)&=\sum a_m(x)\,v_z^m(z)e^{i\xi_mx}\\T_{xx}^1(x,z)&=\sum a_m(x)\,\sigma_{xx}^m(z)e^{i\xi_mx}\\T_{xz}^1(x,z)&=\sum a_m(x)\,\sigma_{xz}^m(z)e^{i\xi_mx}\\T_{zz}^1(x,z)&=\sum a_m(x)\,\sigma_{zz}^m(z)e^{i\xi_mx}\end{aligned} \tag{48}$$

Substituting Eqs. (47) and (48) into the first term of the left hand side of Eq. (41) leads to

$$\begin{aligned}&\frac{\partial}{\partial x}\sum a_m(x)\left[\widetilde{v_x^n}(z)\sigma_{xx}^m(z)+\widetilde{v_z^n}(z)\sigma_{xz}^m(z)\right.\\&\left.+v_x^m(z)\widetilde{\sigma_{xx}^n}(z)+v_z^m(z)\widetilde{\sigma_{xz}^n}(z)\right]e^{i(\xi_m-\widetilde{\xi_n})x}\\&+\frac{\partial}{\partial z}\left[\widetilde{v_x^n}(z)T_{xz}^1(z)+\widetilde{v_z^n}(z)T_{zz}^1(z)\right.\\&\left.+V_x^1(z)\widetilde{\sigma_{xz}^n}(z)+V_z^1(z)\widetilde{\sigma_{zz}^n}(z)\right]e^{-i\widetilde{\xi_n}x}=0\end{aligned} \tag{49}$$

Integrating with respect to z along the entire thickness D, and applying the boundary condition T_{xz}^l, one has

$$\begin{aligned}&\frac{\partial}{\partial x}\sum a_m(x)\,e^{i(\xi_m-\widetilde{\xi_n})x}\\&\int_0^D\left(\widetilde{v_x^n}(z)\sigma_{xx}^m(z)+\widetilde{v_z^n(z)}\sigma_{xz}^m(z)+v_x^m(z)\widetilde{\sigma_{xx}^n}(z)\right.\\&\qquad\left.+v_z^m(z)\widetilde{\sigma_{xz}^n}(z)\right)dz\\&+e^{i(\xi_m-\widetilde{\xi_n})x}\left[\widetilde{v_x^n}(z)T_{xz}^1(z)+\widetilde{v_z^n}(z)T_{zz}^1(z)\right.\\&\qquad\left.+V_x^1(z)\sigma_{xx}^n(z)+T_z^1(z)\sigma_{zz}^n(z)\right]\Big|_0^D\\&=P_{nn}\frac{\partial}{\partial x}\sum a_n(x)+\widetilde{v_x^n}(0)T_{xz}^1(0)e^{i\widetilde{\xi_n}x}=0\end{aligned} \tag{50}$$

Then

$$\frac{\partial}{\partial x}a_n(x)=-\frac{\widetilde{v_x^n}(0)T_{xz}^1(0)e^{i\widetilde{\xi_n}x}}{P_{nn}} \tag{51}$$

Integrating the above equation with respect to x leads to

$$\begin{aligned} a_n(x) &= -\int_e^x \frac{\widetilde{v_x^n}(0) T_{xz}^1(0) e^{i\widetilde{\xi_n}x}}{P_{mn}} dx \\ &= -\frac{\widetilde{v_x^n}(0)}{P_{mn}} \int_e^x T_{xz}^1(0) e^{i\widetilde{\xi_n}x} dx \end{aligned} \tag{52}$$

where e can be determined by the excitation condition. For the excitation generated by infinite long PWAS of $2a$ width shown in Fig. 1, the boundary condition is

$$T_{xz}(x) = T_a[\delta(x-a) - \delta(x+a)] \tag{53}$$

Therefore

$$\begin{aligned} a_n(x) &= -\frac{\widetilde{v_x^n}(0)}{P_{mn}} a T_a \left(e^{i\widetilde{\xi_n}a} - e^{-i\widetilde{\xi_n}a}\right) \\ &= -2iT_a \frac{\widetilde{v_x^n}(0)}{P_{mn}} \sin\left(\widetilde{\xi_n}a\right) \end{aligned} \tag{54}$$

The corresponding displacement and strain wave field components of the n^{th} mode are then calculated as

$$\begin{aligned} u_x^n(x,z) &= \frac{-2iaT_a\widetilde{v_x^n}(0)}{P_{nn}} sin\left(\widetilde{\xi_n}a\right) u_x^n(z) e^{i\xi_n x} \\ \varepsilon_{xx}^n(x,z) &= \frac{\partial u_x^n}{\partial x} \\ &= 2aT_a\widetilde{\xi_n} \frac{\widetilde{v_x^n}(0)}{P_{nn}} sin\left(\widetilde{\xi_n}a\right) u_x^n(z) e^{i\xi_n x} \end{aligned} \tag{55}$$

Eq. (55) is commonly referred to as the Lamb wave displacement/strain tuning curves. It should be noted that T_a depends on the external excitation voltage V. If V is a unit excitation, then it is equivalent to the structural transfer function up to the sensing point located at x. For physical applications, according to the direct piezoelectric effect, the strain can be used to approximate the PWAS voltage output according to Eq. (6) as $V_{out} = -\varepsilon_{ISA} t_a / d_{31}$. However, the strain corresponds to a discrete point while any PWAS is of limited size. Therefore, a smaller PWAS results in a more accurate estimate of the strain field. It should also be noted that the above formulae apply only to Lamb/Rayleigh waves. For the shear horizontal (SH) waves, formulae could be derived in a similar way.

4.4 Wave field calculation

In practice, a short period excitation, such as tone bursts containing broad frequency components are commonly used. The response frequency spectrum is obtained by multiplying the frequency spectrum of the excitation by the transfer function of the corresponding response. The time domain responses are then calculated by the inverse Fourier transform.

In the derivations of this section, especially in Eq. (50), the orthogonality relations of the wave modes are utilized. This is the essential precondition of the NME method. As a matter of fact, this method is valid for all waves whose mode shapes are mutually orthogonal. In bounded waves guides, either in the plate-like structures studied in this paper or in the prism-like structures such as the rail track, the orthogonality relations of the wave modes holds true according to the reciprocity relation (Pau 2018), therefore the NME method can be also applied.

5. Wave field in single-layer CFRP plate

In this section, the strain output of a free CFRP plate is calculated following the procedures detailed above. The analytical result is validated by the numerical and experimental studies.

5.1 Specimen setup

The CFRP plate is the product of the Tyfo® UC composite laminate strip system of 1016 mm ×101.6 mm × 1.4 mm as shown in Fig. 3. The fiber direction is chosen as x, the perpendicular to the fiber direction as y, and the thickness direction as the z direction. The material properties are listed in Table 1. These data are obtained from the material characterization using ultrasonic immersion technique. This type of CFRP is commonly used to strengthen civil engineering structures through providing additional tensional strength (Petrou *et al.* 2008). The surface bonded circular PWAS is made of Steminc SM412 with a 7-mm diameter and 0.5-mm thickness. In practice a circular PWAS will generate circular- (in isotropic media) or quasi-circular/elliptical (in anisotropic media) wave fields in the structure. In the unidirectional CFRP plate, the wave field along the fiber direction is often used for SHM applications. Therefore, the wave field along the fiber direction could be assumed as straight crested and y-invariant and can be used to approximate the response of the circular PWAS aligned along the fiber direction.

The phase-velocity number dispersion curves in the fiber direction (0°) and the transverse direction (90°) are shown in Fig. 4. As shown in the figure, the phase velocities

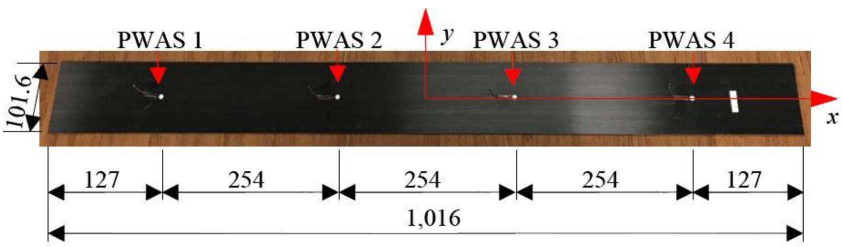

Fig. 3 Experimental specimen (unit: mm)

Table 1 Material properties of the specimens

Material	Parameter	Value
CFRP	Stiffness matrix	$C=\begin{bmatrix} 165.82 & 4.88 & 4.88 & 0 & 0 & 0 \\ & 13.04 & 6.46 & 0 & 0 & 0 \\ & & 13.04 & 0 & 0 & 0 \\ & & & 3.96 & 0 & 0 \\ & \text{symm.} & & & 5.54 & 0 \\ & & & & & 5.54 \end{bmatrix}$ GPa
	Density	1560 kg/m^3
Epoxy	Young's modulus	1.2 GPa
	Density	1200 kg/m^3
	Poisson's ratio	0.38
Concrete	Young's modulus	34.4 GPa
	Density	2500 kg/m^3
	Poisson's ratio	0.2

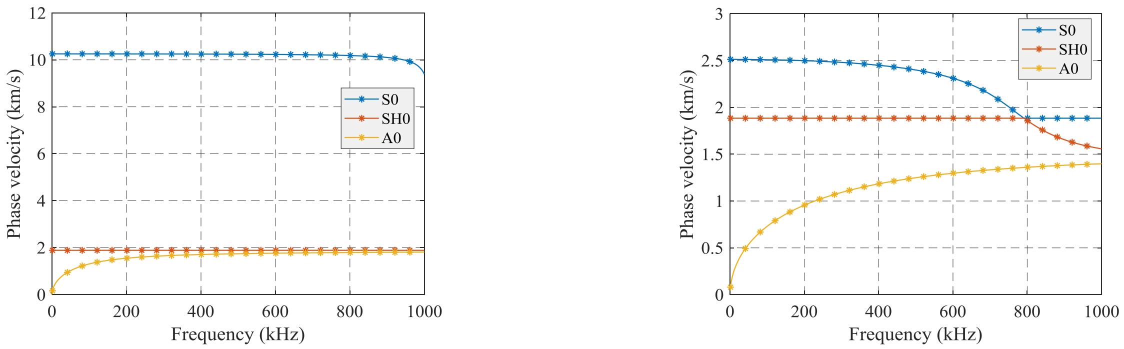

(a) Fiber direction (0°) (b) Transverse direction (90°)

Fig. 4 Phase velocity dispersion curve in different directions

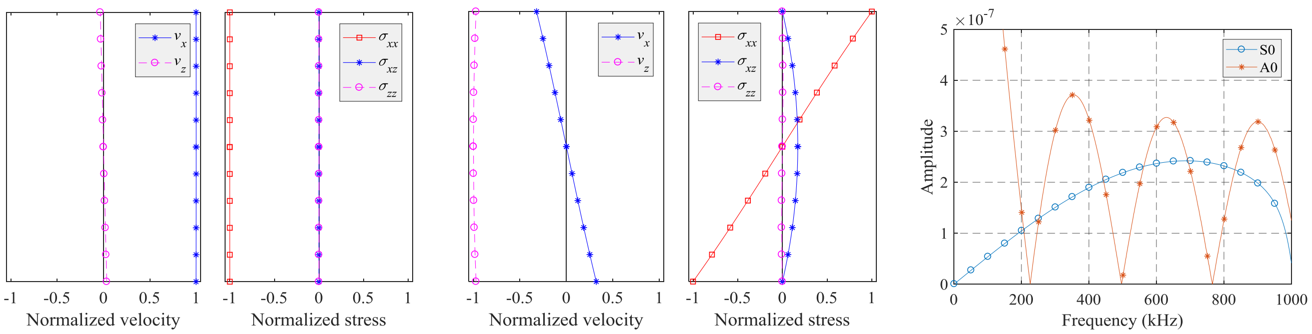

(a) Mode shapes of S0 mode at 60 kHz (b) Mode shapes of A0 mode at 60 kHz (c) ε_{xx} tuning curves [Eq. (55)]

Fig. 5 Mode shapes and tuning curves

of the two modes differ significantly, especially the first symmetric (S0) mode. The phase velocity of S0 mode in the 0° direction is more than 4 times that in the 90° direction at frequencies lower than 600 kHz. The following theoretical demonstrations will be conducted in the 0° direction.

5.2 Theoretical calculation

The theoretical calculations here are based on the steady-state wave field assumption and give the direct incident wave field results only. No reflections or scatters from specimen imperfection or damage are considered at this stage.

The S0 and A0 wave velocity and displacement mode shapes in the 0° direction at 60 kHz are given in Fig. 5(a) and (b). Based on the mode shapes, the tuning curves of the strain at 254 mm away from the PWAS center is shown in Fig. 5(c). When the excitation frequency is relatively low (≤ 200 kHz), the A0 mode tuning curve has a much larger amplitude than that of the S0 mode, indicating that the time history response of the A0 wave packet has a larger amplitude than the S0 mode.

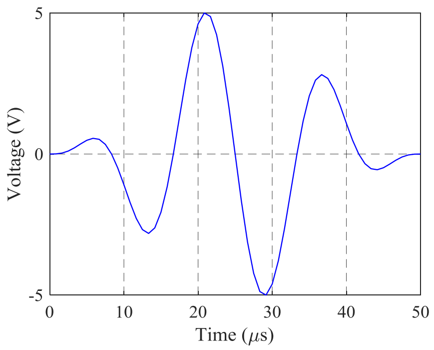

(a) Wave form

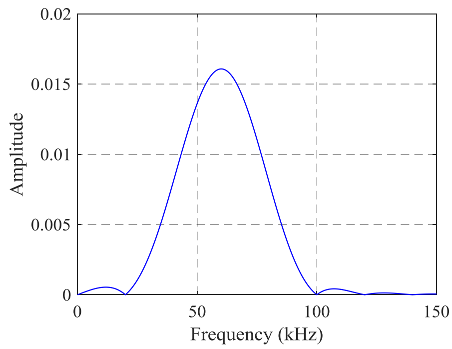

(b) Frequency spectrum

Fig. 6 Excitation wave

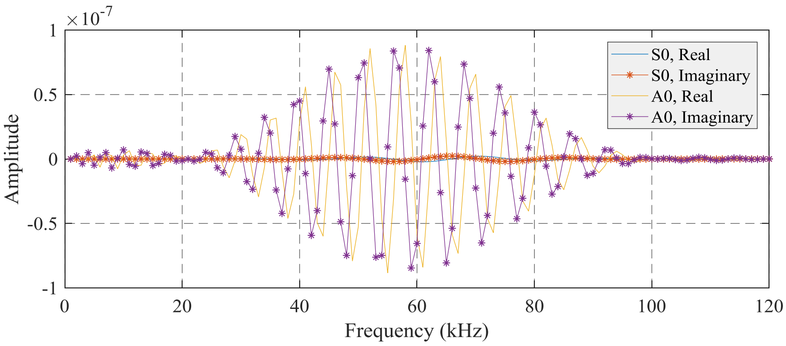

(a) ε_{xx} response spectrum

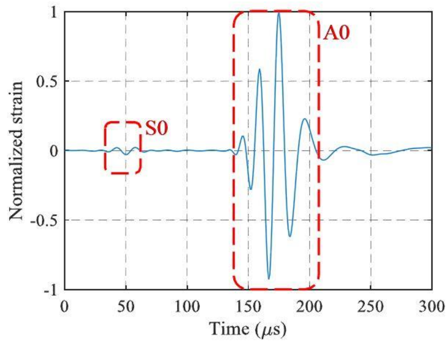

(b) Normalized ε_{xx} time history

Fig. 7 ε_{xx} frequency and time domain responses at 254 mm: (a) ε_{xx} response spectrum; (b) normalized ε_{xx} time history

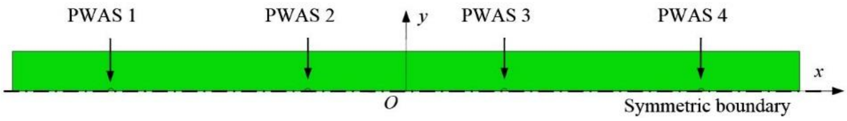

(a) PWAS excitation location and sensing point

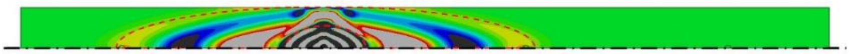

(b) ε_{xx} field at 33.3 μs

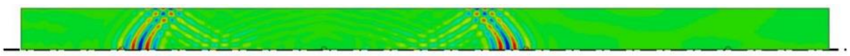

(c) ε_{xx} field at 160 μs

Fig. 8 FEA model and ε_{xx} fields of the CFRP plate

The time history response also depends on the excitation time history. A three-count Hanning-windowed tone burst excitation of a 60 kHz center frequency and a 10 V peak-to-peak amplitude is applied on the PWAS. The excitation waveform and corresponding frequency spectrum are shown in Fig. 6. This center frequency is chosen to balance the amplitudes of the wave packets and the propagation distance of the waves in this study (Other optimal center frequencies can also be chosen in other applications). By multiplying the excitation frequency spectrum shown in Fig. 6(b) and the tuning curve shown in Fig. 5(c), the strain frequency response spectrum is obtained and shown in Fig. 7(a). The time domain response is further obtained as shown in Fig. 7(b). Due to the relative long travelling distance (254 mm), the S0 wave packet and A0 wave packet are completely separated. As stated above, the S0 wave packet has a much smaller amplitude than that of the A0 mode. The low-amplitude tail also follows the A0 wave packet, which has a long period, possibly due to the error in calculating the tuning curves.

5.3 FEA validation

To validate the theoretical calculation, the wave field of the specimen is calculated using the commercial FEA package Abaqus (Dassault Systèmes Simulia Corp. 2012). The excitation shown in Fig. 6 is applied on PWAS 2.

The plate material and PWAS are the same as those in the theoretical calculation. The bottom surface of the PWAS is coupled to the plate with the "Tie" constraint type, such that all six degrees of freedom of the nodes in the interface are identical. The C3D8E coupled field elements are chosen for the PWAS and C3D8R elements for the plate. The wavelength in the fiber direction is approximately 83.3 mm at 120 kHz (double the center frequency). The element size should be smaller than 1/20 of the wavelength to meet the convergence requirement. In this regard, the maximum mesh size of the PWAS is 0.5 mm and the plate is discretized as 1 mm × 1 mm × 0.35 mm. Due to the symmetry, half of the specimen is simulated with the symmetric boundary condition, as shown in Fig. 8(a). The reflections from the horizontal (plane y = 50.8 mm) and vertical ends (planes x = ± 508 mm) will exist, especially reflections from the former. The ε_{xx} strain field at 33.3 μs and 160 μs are respectively plotted in Figs. 8(b) and (c). In Fig. 8(b), two wave packets consisting of different wavelengths are observed, and the wave packet with longer wavelengths enclosed by the dashed curves is the S0 wave packet. From Fig. 8(b), the SH0 mode wave velocity is relatively closer to the A0 wave velocity at low frequency, therefore SH0 wave packet merges with A0. At the same time, the SH wave in the direction close to 0° has few ε_{xx} component due to the propagation direction. Therefore, the remaining ε_{xx}wave fluctuations are mainly the A0 wave packet. The color of the A0 wave packet is more saturated than that of the S0 mode, indicating it has a higher amplitude. In this subfigure there is no reflected wave field. In Fig. 8(c), where the entire color scale is set to a larger strain range to realize a better wave field plot, both wave packets have experienced multiple reflections at different boundaries, resulting in a scattered wave field. The voltage response of PWAS 1 is shown in Fig. 9. The wave packet shapes are generally in accordance with the theoretical calculation, except for the reflections from the specimen borders after the direct incident wave packets. Additional comparisons with experimental results are presented next in the experimental validation section.

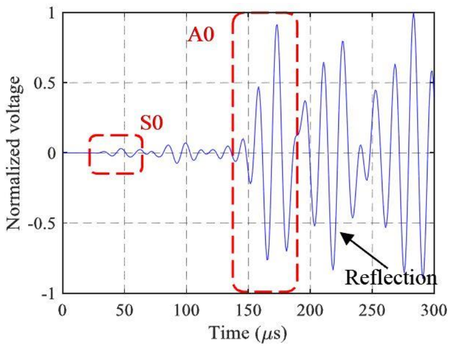

Fig. 9 Normalized voltage response of PWAS 1

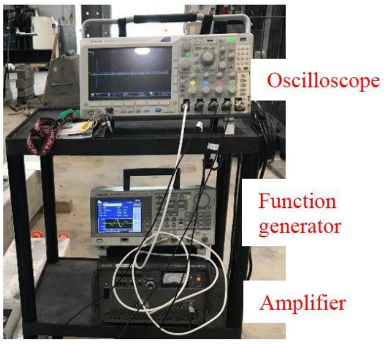

Fig. 10 Experimental setup

5.4 Experimental validation

The specimen shown in Fig. 3 was tested in the laboratory. The voltage excitation shown in Fig. 6(a) generated by a Tektronix AFG3052C dual channel function generator is first amplified to 140 V peak-to-peak by an NF HSA4014 high-speed bipolar amplifier, and then applied to PWAS 2. The voltage response was collected by a Tektronix DPO5034 digital phosphor oscilloscope that was in synchronization with the excitation. These devices are shown in Fig. 10. The voltage response of PWAS 1 is given in Fig. 11(a). PWAS 3 presents similar direction incident wave packets to the PWAS 1 response, except the different reflective wave packet as PWAS is close to the reflection plane of x = -508 mm. In Fig. 11(b), the normalized ε_{xx} obtained from NME calculation and FEA as well as the normalized voltage of PWAS 1 are compared. The directed wave packets of the three waves match well for both the A0 and S0 wave packets. The FEA presents different reflective results from the experiment. The possible reason is that the material properties are not accurate, which influences the

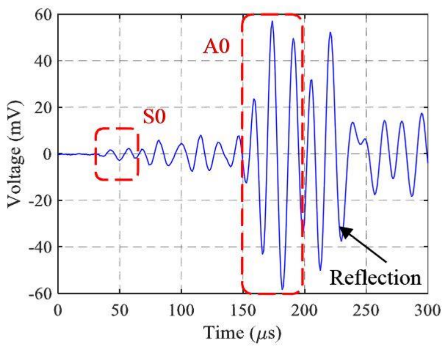

(a) Normalized PWAS 1 output

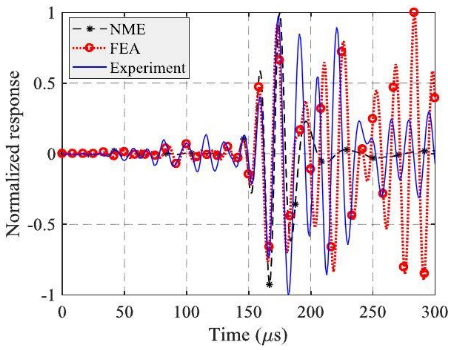

(b) Results comparison

Fig. 11 Normalized voltage response of PWAS 1 and results comparison

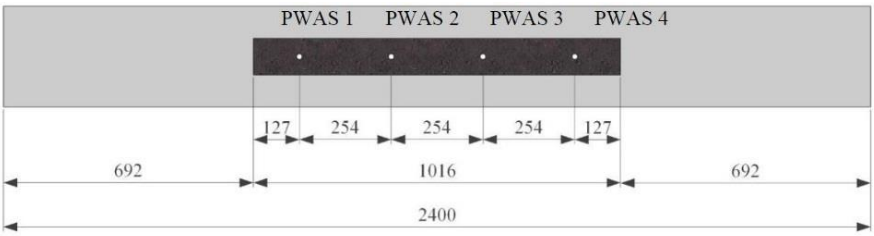

(a) Schematic of the complete test specimen (unit: mm)

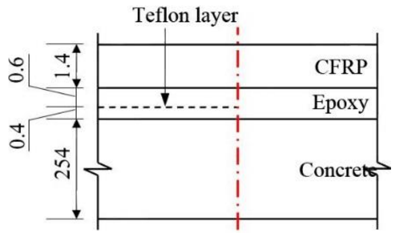

(b) Front view schematic (unit: mm)

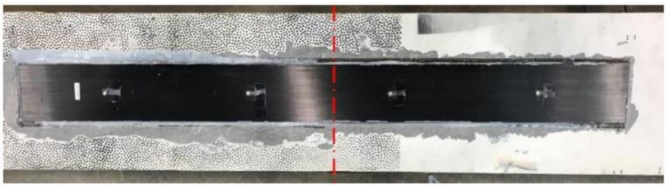

(c) Specimen with Teflon inserted

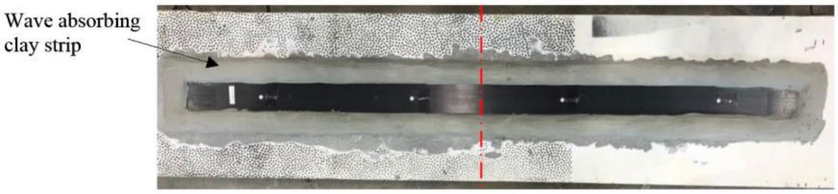

(d) Specimen with Teflon removed and wave absorbing clay applied

Fig. 12 Experimental setup

reflective waves. In addition, the FEA presents the strain of a single point while in the experiment, the dimension of the PWAS also affects the results.

6. Wave field in bonded and debonded CFRP plates

In the previous section, the CFRP plate is in a free state, while its typical and common application is to strengthen civil engineering structures. The enhanced structural performance is achieved when good bonding conditions are secured. The above specimen was then attached to a concrete beam through a Tyfo® TC epoxy layer (roughly 1 mm thick). The prestressed concrete beam specimen is 2400 mm in length with a cross sectional area of A_b = 280 mm × 280 mm and is prestressed by four 7-wire low relaxation strands of diameter d_s = 12.7 mm. The concrete has 48.26 MPa minimum 28-day strength and 27.58 MPa minimum strength at the time of strand release and the mix design used in the fabrication of the concrete beam is the high strength reduced modulus reported by Zeitouni *et al*. (2018). The complete CFRP plated concrete beam system is shown in Fig. 12(a). During the CFRP-attaching stage, a thin layer of Teflon (0.05 mm thick) was inserted in the epoxy layer on the left half span of the CFRP. The front view schematic is shown in Fig. 12(b) and the experimental top view in Fig. 12(c). After the epoxy was fully cured, the Teflon layer was removed, which introduced an artificially generated debonding zone in the left half span. A strip of modeling clay was then attached on the perimeter of the top surface of the entire CFRP plate to absorb the reflective waves to simulate the non-reflective boundary condition, as shown in Fig. 12(d). This leaves the left half of the CFRP in a debonded state while the right half span bonded state. The excitation for the left half-span was applied on PWAS 2 and collected on PWAS 1. The data acquisition of the right half span has a generally symmetric configuration with the excitation applied on PWAS 4 and collected at PWAS 3.

6.1 Left half span (debonded condition)

6.1.1 Theoretical calculation

In the left half span, the Lamb waves propagated in the CFRP–epoxy double layer plate. The information of the epoxy is listed in Table 1. Its precise thickness is difficult to control. During the attachment stage, the desired thickness is 1 mm and after removing the Teflon, the thickness of the epoxy attached on the CFRP plate is around 0.6 mm. The epoxy surface is not smooth and the thickness is not even.

Based on the derivations in Section 4, the corresponding analytical results are given in Fig. 13. The phase-velocity dispersion curve in the left half span is given in Fig. 13(a). As the frequency is low (< 200 kHz), three modes exist: 1st is similar to the S0 mode in the single layer plate, 2nd to the SH0 mode and 3rd to the A0 mode. Again, as the PWAS

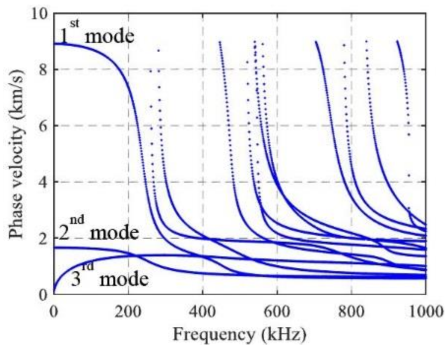

(a) Phase velocity dispersion curve

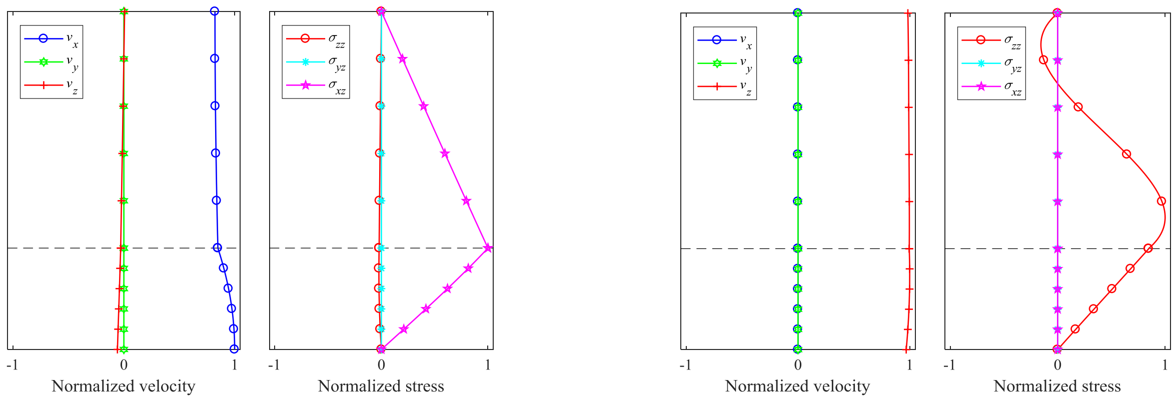

(a) 1st mode shapes at 60 kHz (c) 3rd mode shapes at 60 kHz

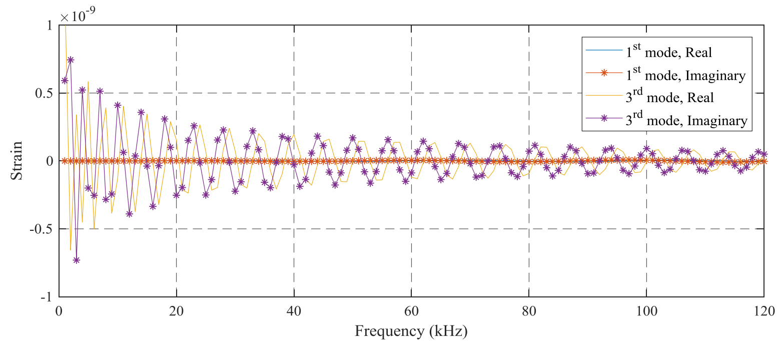

(d) Strain tuning curve at PWAS 1 [Eq. (55)]

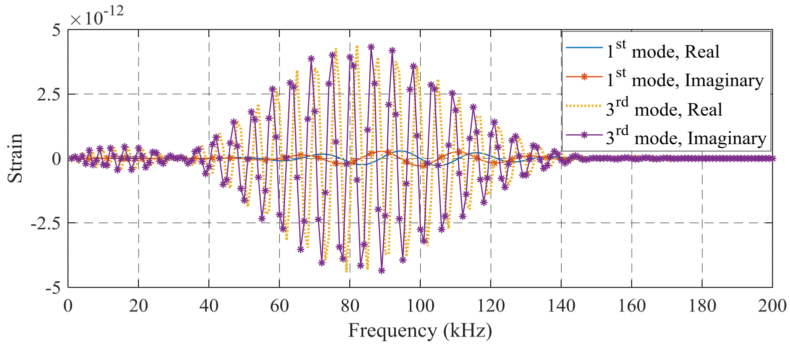

(e) ε_{xx} response spectrum at PWAS 1

Fig. 13 Theoretical calculation of strain in the left half span

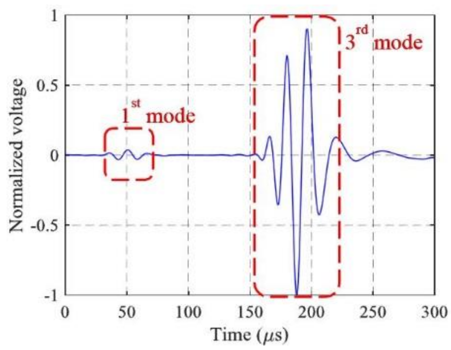

(f) Normalized ε_{xx} time history at PWAS 1 center

Fig. 13 Continued

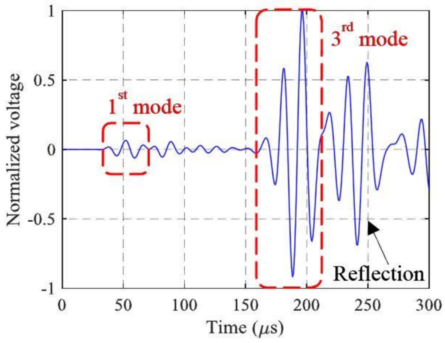

Fig. 14 Normalized voltage from FEA

cannot excite the SH waves in the configuration given in this study, the 2nd mode will not be considered. Figs. 13(b) and (c) present the normalized velocity and stress mode shapes of the 1st and 3rd modes at 60 kHz, respectively. Then the ε_{xx} tuning curve and response spectrum are given in Figs. 13(d) and (e), followed by the normalized time history response in Fig. 13(f).

6.1.2 FEA results

The FEA model of the CFRP-epoxy is similar to the model in Section 1.1, except that a 0.6 mm thick epoxy layer is added on the bottom surface of the CFRP plate. The normalized voltage is simulated and plotted in Fig. 14. The reflections from the specimen boundaries after the direct incident wave packets are observed after the first and third modes.

6.1.3 Experimental results

In the left half span, the measured normalized voltage output of PWAS 1 is given in Fig. 15(a). Owing to the wave absorbing clay, majority of the reflected waves vanish. The normalized strain obtained with NME method and FEA, and the experimental voltage at PWAS 1 is compared in Fig. 15(b). Good agreement has been obtained. The effectiveness of the NME method is thus validated.

6.2 Right half span (bonded condition)

6.2.1 Theoretical calculation

In the right half span, the excitation shown in Fig. 6 is applied on PWAS 3 and the response of PWAS 4 is measured. The waves propagate in the CFRP–epoxy–concrete triple-layer media. As the thickness of the concrete layer is significantly larger than those of the CFRP and epoxy layers, the waves are confined in the surface zone, which is referred to as the Rayleigh–Lamb waves. The phase-velocity dispersion curves are calculated using the GMM and plotted in Fig. 16(a). Different from the above demonstrated free CFRP and CFRP-epoxy cases in which at least two modes exist at low frequencies, only one mode presents at frequencies lower than 140 kHz. The velocity and stress mode shapes are calculated and depicted in Fig. 16(b). On the basis of the mode shapes, the ε_{xx} tuning curves [Eq. (52)] and ε_{xx} response spectrum at the center of the PWAS 4 are calculated using the NME method and

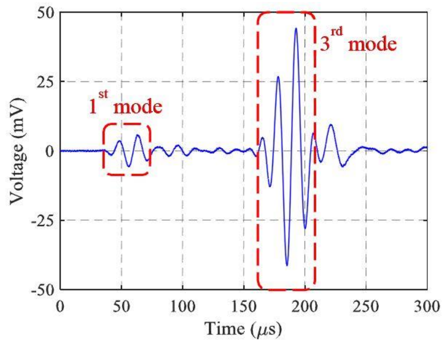

(a) Voltage of PWAS 1

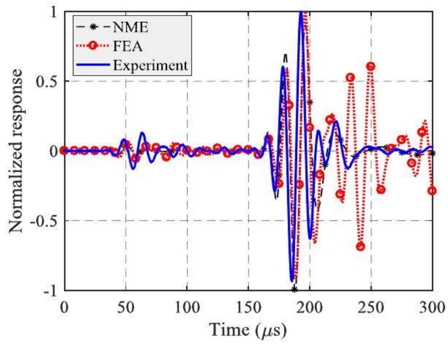

(b) Comparison of normalized outputs

Fig. 15 Measured responses and comparison of normalized results at PWAS 1

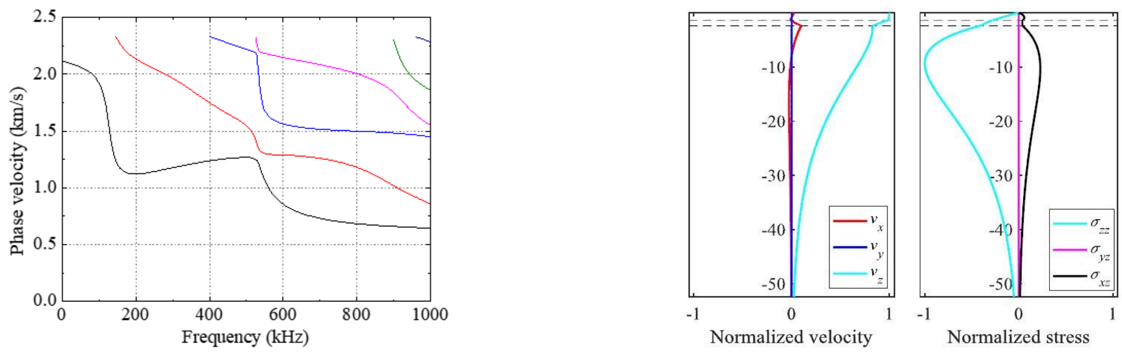

(a) Phase velocity dispersion curves (b) Velocity and stress mode shapes at 60 kHz

Fig. 16 Dispersion curves and mode shapes

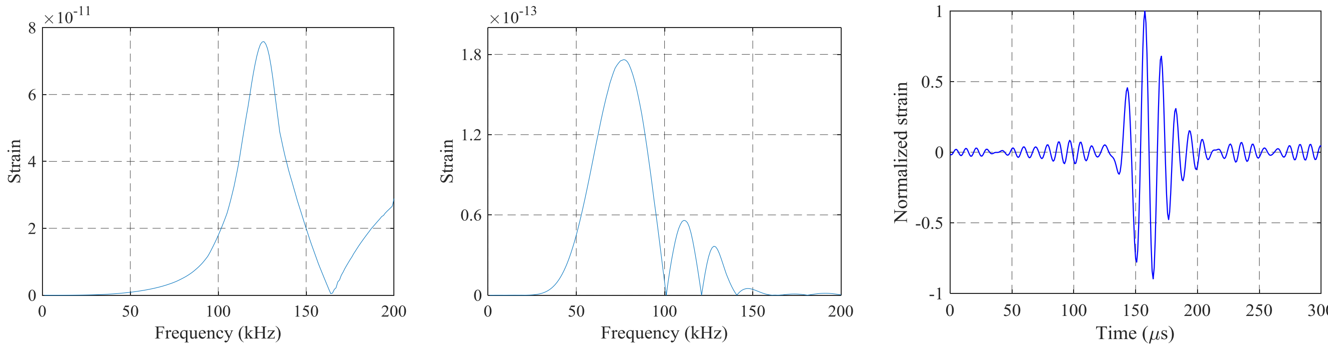

(a) Phase velocity dispersion curves (b) Velocity and stress mode shapes at 60 kHz (c) Normalized ε_{xx} under the PWAS 4 center

Fig. 17 Calculated structural responses

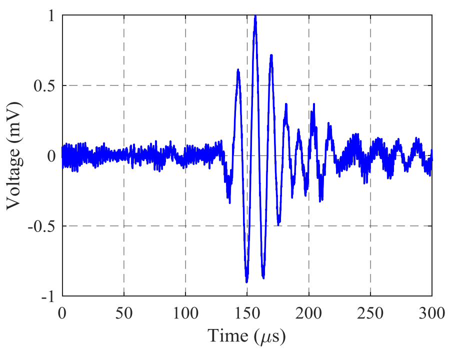

Fig. 18 Voltage of PWAS 4

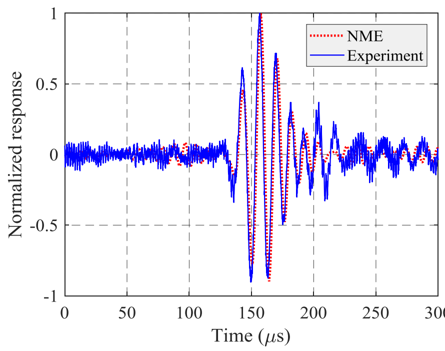

Fig. 19 Comparison of theoretical and experimental structural responses

plotted in Figs. 17(a) and (b) respectively. Consequently, the time domain response is then calculated using the inverse Fourier transform and shown in Fig. 17(c). Unexpected fluctuations before and after the main packets are observed, which is possibly due to the numerical errors in the calculating the dispersion curves and the mode shapes using the GMM, rather than the NME calculation process.

6.2.2 Experimental results

In the right half span, the excitation was applied on the PWAS 3 and the voltage on the PWAS 4 was collected as plotted in Fig. 18. For comparison, the normalized strain is calculated using the NME method and the normalized voltage of the PWAS 4 is plotted in Fig. 19. Despite the undesired fluctuations in the theoretical calculation, the main packet matches well with the experimental results. Therefore, the NME method can calculate the wave field in bonded CFRP plates accurately.

6.3 Comparison of PWAS responses under bonded and debonded conditions

The wave fields in the free, bonded and debonded CFRP plates presented different wave packet shapes and propagation time, which can facilitate monitoring the CFRP bonding condition. For better understanding the influence of the CFRP bonding condition on the wave field response, the same excitation was applied on PWAS 2 and 3 respectively and the wave fields induced by them are respectively collected at PWAS 1 and 4 as shown in Fig. 20(a). The results of PWAS 1 before and after the Teflon layer was

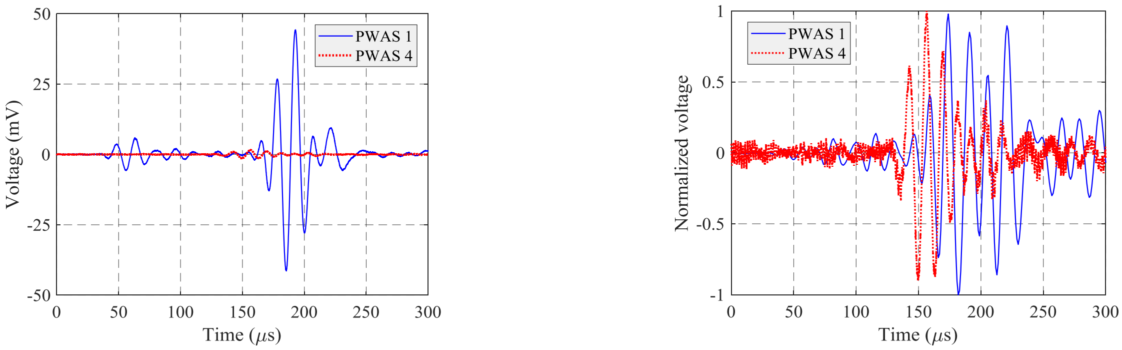

(a) Voltage of PWAS 1 and PWAS 4 (b) Normalized voltage

Fig. 20 Voltage of PWAS 1 and PWAS 4

Table 2 Summary of wave propagation features

CFRP condition	Amplitude (% of Case 1)	Arrival time of peak
Case 1: Free CFRP	80.14 mV (100%)	173.8 μs
Case 2: Bonded CFRP	1.61 mV (2.0%)	156.5 μs
Case 3: Debonded CFRP	44.27 mV (55.1%)	192.9 μs

removed are not compared because the Teflon layer in the epoxy layer introduced another wave reflection interface, which differs from the typical bonded condition. Under the same amplitude excitation, PWAS 4 in the CFRP perfectly bonded zone has a significantly smaller amplitude than PWAS 1 in the debonded zone, around 1/27 to be specific. The normalized results are shown in Fig. 20(b), in which the difference in the wave travelling time is obvious. For a perfectly bonded CFRP plate, the guided waves leak into the concrete. When the epoxy debonds from the concrete, the waves are confined in the CFRP and epoxy layers, and their propagation properties change in terms of the amplitude and travelling time. In practical applications, both the amplitude and travelling time of wave packet can be used to evaluate the CFRP bonding condition. To understand the wave field change due to the CFRP bonding condition quantitatively, Table 2 summarizes the peak values and their arrival time. The response of the free CFRP plate is chosen as the baseline (Case 1). When the CFRP plate is bonded to the RC beam (Case 2), the amplitude drops to around 2% of Case 1, whereas the wave propagation time reduced. When the CFRP plate debonds from the RC beam (Case 3), the wave energy cannot leak into the RC beam, and thus, the amplitude resumes to 63.1% of Case 1. However, the propagation time considerably increased.

In practice, the wave packet shape, peak amplitude and arrival time of the peak value can facilitate the CFRP bonding condition evaluation. The evaluation can be based on the perfect bonding condition data (Case 2) or can be baseline-free. When the data of the perfect bonded cases are available, it is observed that the wave amplitude increases significantly due to the inability of the wave energy to propagate to the concrete. In this case the wave propagation time will increase. In contrast, when the baseline data is not available, the actual wave guide in which the waves are actually propagating can be approximated by fitting the theoretical calculation with the experimental measurement.

7. Conclusions

The Lamb wave field generated by surface mounted PWAS in the multi-layer plate made of generally anisotropic material is studied using the NME method. The wave field in anisotropic material is first given and the NME formulae are derived. Then the wave field in a unidirectional CFRP composite plate is calculated with the NME and validated by FEA and experimental results. In particular, the CFRP plate in bonded and debonded conditions were simulated on an experimental prestressed concrete beam. Their wave fields excited by PWAS are compared. Both the wave packet amplitude and travelling time can serve for the evaluation of the CFRP bonding condition.

In this study, the wave field excited by a circular PWAS is considered under the straight-crested wave field assumption, which is a simplification in each individual direction. One distinguished difference between the circular- and straight- crested wave field is that geometry spreading does not exist in the latter. Therefore the amplitude decrease in the FEA model and experiment is not considered in the NME method. Consequently, only the normalized results are compared in this study. The geometry spreading effects could be revised by introducing an exponential decaying function. The material damping can also be considered similarly, or alternatively, a negative imaginary part can be introduced in the material stiffness matrix. In this paper, the damping is not considered since the damping ratio in the fiber direction is quite small. In practical applications, the wave field in the CFRP plate and CFRP-epoxy plate (the debonded case) could be established as a baseline for the CFRP bonding condition evaluation.

Acknowledgments

This research was supported by The Hong Kong Polytechnic University Research Grant (No. 1-BBAG) and the RGC Theme-based Research Scheme (Project No. T22-

502/18-R). The generous donation of Tyfo TC epoxy from the Fyfe Co. LLC is highly appreciated. The first author is grateful to the Research Grants Council of the Hong Kong Special Administrative Region for the Hong Kong PhD Fellowship Award.

References

Achenbach, J. and Xu, Y. (1999), "Wave motion in an isotropic elastic layer generated by a time-harmonic point load of arbitrary direction", *J. Acoust. Soc. Am.*, **106**(1), 83-90 https://doi.org/10.1121/1.427037

Auld, B.A. (1990), *Acoustic Fields and Waves in Solids,* Vol. Ii, Krieger Publishing Company, Malabar, FL, USA.

Bai, H., Zhu, J., Shah, A.H. and Popplewell, N. (2004), "Three-dimensional steady state Green function for a layered isotropic plate", *J. Sound Vib.*, **269**(1), 251-271. https://doi.org/10.1016/S0022-460X(03)00071-3

Barouni, A.K. and Saravanos, D.A. (2016), "A layerwise semi-analytical method for modeling guided wave propagation in laminated and sandwich composite strips with induced surface excitation", *Aerosp. Sci. Technol.*, **51**, 118-141. https://doi.org/10.1016/j.ast.2016.01.023

Chimenti, D.E. (2014), "Review of air-coupled ultrasonic materials characterization", *Ultrasonics*, **54**(7), 1804-1816. https://doi.org/10.1016/j.ultras.2014.02.006

Dassault Systèmes Simulia Corp. (2012), Abaqus 6.12 Analysis User's Manual.

Giurgiutiu, V. (2005), "Tuned Lamb wave excitation and detection with piezoelectric wafer active sensors for structural health monitoring", *J. Intel. Mater. Syst. Struct.*, **16**(4), 291-305. https://doi.org/10.1177/1045389X05050106

Giurgiutiu, V. (2007), *Structural Health Monitoring with Piezoelectric Wafer Active Sensors: With Piezoelectric Wafer Active Sensors*, Elsevier.

Giurgiutiu, V. (2014), *Structural Health Monitoring with Piezoelectric Wafer Active Sensors*, Elsevier/Academic Press, Amsterdam, Boston, MA, USA.

Glushkov, E., Glushkova, N. and Eremin, A. (2011), "Forced wave propagation and energy distribution in anisotropic laminate composites", *J. Acoust. Soc. Am.*, **129**(5), 2923-2934. https://doi.org/10.1121/1.3559699

Gopalakrishnan, S., Ruzzene, M. and Hanagud, S. (2011), "Spectral Finite Element Method", In: *Computational Techniques for Structural Health Monitoring*, Springer, pp. 177-217.

Hirao, M. (2017), *Electromagnetic Acoustic Transducers: Noncontacting Ultrasonic Measurements Using Emats*, Springer, Japan.

Kamal, A.M., Lin, B. and Giurgiutiu, V. (2014), "Exact analytical modeling of power and energy for multimode lamb waves excited by piezoelectric wafer active sensors", *J. Intel. Mater. Syst. Struct.*, **25**(4), 452-471. https://doi.org/10.1177/1045389X13498310

Knopoff, L. (1964), "A matrix method for elastic wave problems", *Bull. Seismol. Soc. Am.*, **54**(1), 431-438.

Leckey, C.A., Rogge, M.D. and Parker, F.R. (2014), "Guided waves in anisotropic and quasi-isotropic aerospace composites: Three-dimensional simulation and experiment", *Ultrasonics*, **54**(1), 385-394. https://doi.org/10.1016/j.ultras.2013.05.007

Leckey, C.A.C., Wheeler, K.R., Hafiychuk, V.N., Hafiychuk, H. and Timuçin, D.A. (2018), "Simulation of guided-wave ultrasound propagation in composite laminates: Benchmark comparisons of numerical codes and experiment", *Ultrasonics*, **84**, 187-200. https://doi.org/10.1016/j.ultras.2017.11.002

Lee, J., Park, C. and Kong, C. (2013), "Simultaneous active strain and ultrasonic measurement using fiber acoustic wave piezoelectric transducers", *Smart Struct. Syst., Int. J.*, **11**(2), 185-197. https://doi.org/10.12989/sss.2013.11.2.185

Li, Y. and Thompson, R.B. (1990), "Influence of anisotropy on the dispersion characteristics of guided ultrasonic plate modes", *J. Acoust. Soc. Am.*, **87**(5), 1911-1931. https://doi.org/10.1121/1.399318

Li, L., Haider, M.F., Mei, H., Giurgiutiu, V. and Xia, Y. (2019), "Theoretical calculation of circular-crested Lamb wave field in single-and multi-layer isotropic plates using the normal mode expansion method", *Struct. Health Monitor.*, **19**(2), 357-372. https://doi.org/10.1177/1475921719848149

Liu, G. and Xi, Z. (2001), *Elastic Waves in Anisotropic Laminates*, CRC press.

Loveday, P.W. (2009), "Semi-analytical finite element analysis of elastic waveguides subjected to axial loads", *Ultrasonics*, **49**(3), 298-300. https://doi.org/10.1016/j.ultras.2008.10.018

Lowe, M.J. (1995), "Matrix techniques for modeling ultrasonic waves in multilayered media", *IEEE Transact. Ultrason. Ferroelect. Freq. Control*, **42**(4), 525-542. https://doi.org/10.1109/58.393096

Mei, H. and Giurgiutiu, V. (2018), "Guided wave excitation and propagation in damped composite plates", *Struct. Health Monitor.*, **18**(3), 690-714. https://doi.org/10.1177/1475921718765955

Meitzler, A., Tiersten, H., Warner, A., Berlincourt, D., Couqin, G. and Welsh III, F. (1988), "IEEE standard on piezoelectricity"

Mohseni, H. and Ng, C.T. (2013), "Rayleigh wave for detecting debonding in FRP-retrofitted concrete structures using piezoelectric transducers", *Comput. Concrete, Int. J.*, **20**(5), 583-593. https://doi.org/10.12989/cac.2017.20.5.583

Mohseni, H. and Ng, C.-T. (2019), "Rayleigh wave propagation and scattering characteristics at debondings in fibre-reinforced polymer-retrofitted concrete structures", *Struct. Health Monitor.*, **18**(1), 303-317. https://doi.org/10.1177/1475921718754371

Moulin, E., Assaad, J., Delebarre, C. and Osmont, D. (2000), "Modeling of Lamb waves generated by integrated transducers in composite plates using a coupled finite element–normal modes expansion method", *J. Acoust. Soc. Am.*, **107**(1), 87-94. https://doi.org/10.1121/1.428294

Ng, C.-T. and Veidt, M. (2012), "Scattering characteristics of Lamb waves from debondings at structural features in composite laminates", *J. Acoust. Soc. Am.*, **132**(1), 115-123. https://doi.org/10.1121/1.4728192

Pau, A. (2018), "Derivation of wave mode orthogonality from reciprocity in direct notation", *J. Nondestr. Eval. Diagn. Progn. Eng. Syst.*, **1**(2), 024501. https://doi.org/10.1115/1.4039477

Petrou, M.F., Parler, D., Harries, K.A. and Rizos, D.C. (2008), "Strengthening of reinforced concrete bridge decks using carbon fiber-reinforced polymer composite materials", *J. Bridge Eng.*, **13**(5), 455-467. https://doi.org/10.1061/(ASCE)1084-0702(2008)13:5(455)

Rose, J.L. (2014), *Ultrasonic Guided Waves in Solid Media*, Cambridge University Press, New York, USA.

Santoni, G. (2010), "Fundamental Studies in the Lamb-Wave Interaction between Piezoelectric Wafer Active Sensor and Host Structure During Structural Health Monitoring", Doctor of Philosophy, University of South Carolina, USA.

Santoni, B.G. and Giurgiutiu, V. (2012), "Exact shear-lag solution for guided waves tuning with piezoelectric-wafer active sensors", *AIAA Journal*, **50**(11), 2285-2294. https://doi.org/10.2514/1.J050667

Shen, Y. and Giurgiutiu, V. (2013), "Predictive modeling of nonlinear wave propagation for structural health monitoring with piezoelectric wafer active sensors", *J. Intel. Mater. Syst. Struct.*, **25**(4), 506-520. https://doi.org/10.1177/1045389X13500572

Shen, Y. and Giurgiutiu, V. (2014), "WaveFormRevealer: An analytical framework and predictive tool for the simulation of multi-modal guided wave propagation and interaction with damage", *Struct. Health Monitor.*, **13**(5), 491-511. https://doi.org/10.1177/1475921714532986

Shen, Y. and Giurgiutiu, V. (2016), "Combined analytical FEM approach for efficient simulation of Lamb wave damage detection", *Ultrasonics*, **69**, 116-128. https://doi.org/10.1016/j.ultras.2016.03.019

Sherafat, M.H., Guitel, R., Quaegebeur, N., Lessard, L., Hubert, P. and Masson, P. (2016), "Guided wave scattering behavior in composite bonded assemblies", *Compos. Struct.*, **136**, 696-705. https://doi.org/10.1016/j.compstruct.2015.10.046

Su, Z., Ye, L. and Lu, Y. (2006), "Guided Lamb waves for identification of damage in composite structures: A review", *J. Sound Vib.*, **295**(3-5), 753-780. https://doi.org/10.1016/j.jsv.2006.01.020

Velichko, A. and Wilcox, P.D. (2007), "Modeling the excitation of guided waves in generally anisotropic multilayered media", *J. Acoust. Soc. Am.*, **121**(1), 60-69. https://doi.org/10.1121/1.2390674

Vrettos, C. (2008), "Green's functions for vertical point load on an elastic half-space with depth-degrading stiffness", *Eng. Anal. Bound. Elem.*, **32**(12), 1037-1045. https://doi.org/10.1016/j.enganabound.2007.10.017

Wang, L. and Rokhlin, S.I. (2001), "Stable reformulation of transfer matrix method for wave propagation in layered anisotropic media", *Ultrasonics*, **39**(6), 413-424. https://doi.org/10.1016/S0041-624X(01)00082-8

Wang, L. and Yuan, F.G. (2007), "Group velocity and characteristic wave curves of Lamb waves in composites: Modeling and experiments", *Compos. Sci. Technol.*, **67**(7), 1370-1384. https://doi.org/10.1016/j.compscitech.2006.09.023

Wang, Z., Qiao, P. and Shi, B. (2017), "A comprehensive study on active Lamb wave-based damage identification for plate-type structures", *Smart Struct. Syst., Int. J.*, **20**(6), 759-767. https://doi.org/10.12989/sss.2017.20.6.759

Weaver, R. and Pao, Y.-H. (1982), "Axisymmetric elastic waves excited by a point source in a plate", *J. Appl. Mech.*, **49**(4), 821-836. https://doi.org/10.1115/1.3162623

Wilcox, P.D. (2003), "Omni-directional guided wave transducer arrays for the rapid inspection of large areas of plate structures", *IEEE Transact. Ultrason. Ferroelect. Freq. Control*, **50**(6), 699-709. https://doi.org/10.1109/TUFFC.2003.1209557

Yu, L. and Giurgiutiu, V. (2008), "In situ 2-D piezoelectric wafer active sensors arrays for guided wave damage detection", *Ultrasonics*, **48**(2), 117-134. https://doi.org/10.1016/j.ultras.2007.10.008

Zeitouni, A.I., Rizos, D.C. and Qian, Y. (2018), "Benefits of high strength reduced modulus (HSRM) concrete railroad ties under center binding support conditions", *Constr. Build. Mater.*, **192**, 210-223. https://doi.org/10.1016/j.conbuildmat.2018.10.124

Zhang, P., Tang, Z., Duan, Y., Yun, C.B. and Lv, F. (2018), "Ultrasonic guided wave approach incorporating SAFE for detecting wire breakage in bridge cable", *Smart Struct. Syst., Int. J.*, **22**(4), 481-493. https://doi.org/10.12989/sss.2018.22.4.481

FC